Symmetry Criteria for the Equality of Interior and Exterior Shape Factors With Exact Solutions

ASME Journal of Heat and Mass Transfer
Online journal at:
https://asmedigitalcollection.asme.org/heattransfer

Symmetry Criteria for the Equality of Interior and Exterior Shape Factors With Exact Solutions

Kyle I. McKee
Department of Mathematics,
Massachusetts Institute of Technology,
Cambridge, MA 02139;
Gulliver Laboratory,
ESPCI Paris, PSL University,
Paris Cedex 05 75231, France
e-mail: kimckee@mit.edu

John H. Lienhard[1]
Fellow ASME
Rohsenow Kendall Heat Transfer Laboratory,
Department of Mechanical Engineering,
Massachusetts Institute of Technology,
Cambridge, MA 02139
e-mail: lienhard@mit.edu

*Lienhard (2019, "Exterior Shape Factors From Interior Shape Factors," ASME J. Heat Mass Transfer-Trans. ASME, **141**(6), p. 061301) reported that the shape factor of the interior of a simply-connected region (Ω) is equal to that of its exterior ($\mathbb{R}^2\backslash\Omega$) under the same boundary conditions. In that study, numerical examples supported the claim in particular cases; for example, it was shown that for certain boundary conditions on circles and squares, the conjecture holds. In this paper, we show that the conjecture is not generally true, unless some additional condition is met. We proceed by elucidating why the conjecture does in fact hold in all of the examples analyzed by Lienhard. We thus deduce a simple criterion which, when satisfied, ensures the equality of interior and exterior shape factors in general. Our criterion notably relies on a beautiful and little-known symmetry method due to Hersch which we introduce in a tutorial manner. In addition, we derive a new formula for the shape factor of objects meeting our N-fold symmetry criterion, encompassing exact solutions for regular polygons and more complex shapes.* [DOI: 10.1115/1.4065741]

Keywords: heat conduction, shape factor, interior, exterior, symmetry, conformal mapping, regular polygons, N*-fold symmetry*

1 Introduction

We consider steady heat conduction inside or outside a planar object. The object has different sections of its boundary at one of two temperatures, with the isothermal sections separated from one another by adiabatic sections. Heat Q (W/m) then flows from the high-temperature portion of the boundary to the low-temperature portion of the boundary at a rate

$$Q = Sk\Delta T \tag{1}$$

where S is the shape factor, ΔT (K) is the temperature difference, and k (W/m K) is the object's thermal conductivity. In two-dimensional problems, S is dimensionless and Q is the heat flow per unit distance normal to the plane. The shape factor is scale invariant and determined exclusively by the particular object's geometry and boundary conditions. Shape factor theory is discussed in detail in Refs. [1–3].

The heat flow can be calculated by solving the Laplace equation in the domain of interest, and then integrating the heat flux exiting the high-temperature portion of the boundary. The shape factor conveniently summarizes the result of such an analysis. In most cases, the shape factor inside a two-dimensional object is easier to compute (analytically or numerically) than the shape factor outside the object, even for an apparently simple object like a square (see, e.g., Ref. [4], Sec. 7.2). Thus, a relationship between the interior and exterior shape factors allows a potentially difficult exterior calculation to be replaced by a more tractable interior calculation or an already known result.

This paper examines the shape factor in two dimensions using techniques from complex analysis and conformal mapping. To proceed mathematically, we precisely define the "object" boundary as a *Jordan curve*: a closed nonself-intersecting curve that divides the plane into an interior region and an unbounded exterior region. For example, the interior and exterior problems relative to a rectangular arc are illustrated in Figs. 1(*a*) and 1(*b*). The boundary is partitioned into a finite number of sections, each prescribed a boundary condition that is either adiabatic (a zero Neumann condition) or isothermal (a constant Dirichlet condition) at one of two temperatures. Sections with different temperatures must be separated by an adiabatic section to ensure a finite rate of heat transfer. However, any number of sections may be at each temperature.

To mathematicians, the shape factor is the reciprocal of the *extremal distance*—a conformal invariant of interest in function theory that is equal to the reciprocal of the Dirichlet energy[2] [5]. Useful properties of the extremal distance are outlined by Ahlfors [5]. When the boundary curve is split into precisely four segments, the extremal distance is equal to the conformal modulus, which was studied by Hersch [6,7] in geometries possessing certain symmetries. By exploiting the Schwarz reflection principle, Hersch derived analytical results for a variety of geometries.

[1]Corresponding author.

Contributed by the Heat Transfer Division of ASME for publication in the Journal of Heat and Mass Transfer. Manuscript received March 27, 2024; final manuscript received May 29, 2024; published online July 4, 2024. Assoc. Editor: Ankur Jain.

[2]For a harmonic function ϕ, defined over a domain $D \subseteq \mathbb{R}^2$, the Dirichlet energy is defined by the following integral over the domain area: $\int_D (\nabla\phi \cdot \nabla\phi) dA$.

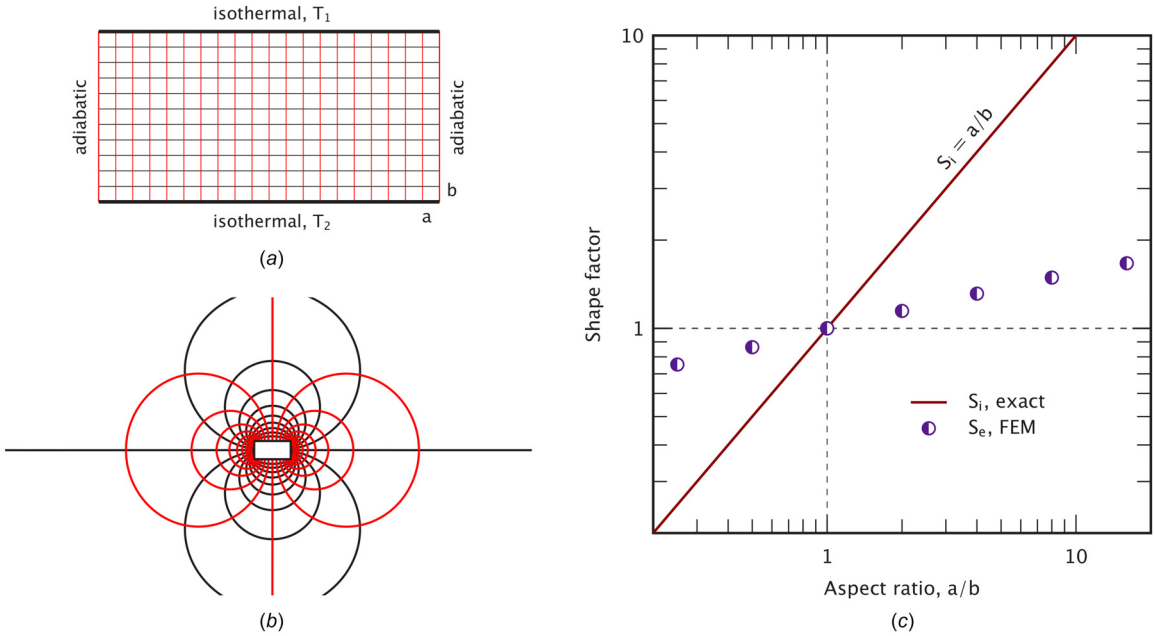

Fig. 1 Interior and exterior shape factor for a rectangle of aspect ratio *a*/*b*. The interior shape factor is exactly *a*/*b*. The exterior values are from FEM calculations (see Appendix A). The interior and exterior shape factors are equal only for the case of a square (*a* = *b*) but unequal for rectangles with *a* ≠ *b*. (*a*) Interior of rectangle, (*b*) exterior of rectangle, and (*c*) interior and exterior shape factors.

More recently, Lienhard [8] made the striking claim that interior and exterior shape factors are always equal. To reach this conclusion, he first used the Riemann mapping theorem to argue that the interior and exterior of a Jordan curve may always be related by a conformal map. Indeed, such a map is guaranteed to exist [9].

Lienhard proceeded by further assuming that each boundary section possessing a given boundary condition is invariant under the interior-to-exterior mapping (up to an overall reflection); we label this assumption A. When true, assumption A does indeed imply that the interior and exterior shape factor problems are conformally equivalent (see Sec. 2), and thus they possess the same shape factor, $S_i = S_e$ [5]. Based on assumption A, Lienhard [8] conjectured that $S_i = S_e$ must always hold. He subsequently analyzed the shape factors for a disk and a square, under various boundary conditions, and found in each case that $S_i = S_e$, thus gaining support for the conjecture. However, we now demonstrate that $S_i = S_e$ need not hold in more general cases than those considered by Lienhard.

Consider the following counterexample: a rectangle with isothermal sides of width a and adiabatic sides with height b. For the case of a square, when $a = b$, it is clear that $S_i = S_e = 1$ as was demonstrated previously [8]. However, for rectangles with $a \neq b$, the two shape factors diverge rapidly, as seen in Fig. 1(*c*).

The purpose of this paper is twofold. First, we shall elucidate why Lienhard's conjecture is not universally true. Second, we provide an additional criterion that does ensure the equality of interior and exterior shape factors. The new criterion relies on a little-known method due to Hersch [7], and we thus take this opportunity to explain that method in an expository manner. In addition, we derive a simple formula for the shape factor of many geometries that satisfy our symmetry criterion.

2 Conformally Equivalent Shape Factor Problems

The failure of assumption A ultimately spoils the conformal equivalence between the interior and exterior problems, as we now describe.

Consider two Jordan curves ∂C and ∂D. Then, let C be the domain defined as either the interior or exterior of ∂C. Let ∂D be the domain defined as either the interior or exterior of ∂D. Suppose that each boundary curve is partitioned into a finite number of sections with each section assigned either a zero Neumann condition or a constant Dirichlet condition at one of two temperatures. Again, sections at different temperatures must be separated by an adiabatic segment to ensure a finite rate of heat transfer.

We say that the two shape factor problems, in the domains C and D, are conformally equivalent if the following criteria hold: (1) the two problem domains are related by a conformal map; and (2) under that mapping, the boundary condition at every image point matches that at the corresponding pre-image point. If two shape factor problems are conformally equivalent, then they possess the same shape factor [5]. The case of interest in this paper is that for which C is the interior and D the exterior of the *same* Jordan curve.

The Riemann mapping theorem guarantees the existence of a conformal map $f(z)$ between the interior and exterior of a Jordan curve, thus guaranteeing the satisfaction of criterion 1. However, the mapping theorem only offers three degrees-of-freedom: one can always construct a map that sends *three* points on the original domain boundary to three chosen points on the target domain's boundary [9]. Note that the choice of the three image points is not completely arbitrary: their order along the boundary must be preserved under the mapping. Once the image locations of three pre-image points are chosen, the map becomes fully specified so that the location of any other point cannot be chosen at will.

Shape factors, however, are determined by a minimum of *four* points, one at the end of each isothermal section. As a result, Riemann's theorem does not guarantee that the boundary conditions are preserved when mapping from the interior to the exterior domain. It follows that the interior and exterior boundary value problems are not necessarily conformally equivalent, meaning that the interior and exterior shape factors are not necessarily equal. An additional constraint or symmetry must be present to ensure that the map leaves the boundary conditions invariant, as will be discussed in Sec. 3. By chance, the specific cases examined by Lienhard each tacitly embodied such symmetries, which led to the incorrect deduction that $S_i = S_e$ must always hold.

3 A Nontrivial Class of Geometries With Equal Interior and Exterior Shape Factors

In this section, we apply a powerful method for analyzing Laplace problems that was described by Hersch in another context [7]. The

method builds upon the Schwarz reflection principle. By application of this method, we deduce a simple criterion that ensures $S_i = S_e$.

After assuming that the domain boundary ∂B (Jordan curve) possesses a certain reflectional symmetry, we proceed to construct a conformal map that translates the interior shape factor problem, defined on int (∂B), into a shape factor problem interior to the unit disk. We similarly translate the exterior shape factor problem into a problem interior to the unit disk. Under further symmetry conditions on the boundary condition placements, we demonstrate that both shape factor problems (interior and exterior to ∂B) map to the same problem on the interior of the unit circle, and thus possess identical shape factors.

3.1 Schwarz Reflection Principle: Hersch Sector Reflections and the Interior Problem.

The Schwarz reflection principle may be stated as follows [9].

Theorem 1 (Schwarz Reflection). *Consider a domain W symmetric with respect to the real axis, where we define $W^+ = W \cap \{\mathrm{Im} z > 0\}$ and $W^- = W \cap \{\mathrm{Im} z < 0\}$ and $z \in \mathbb{C}$. Let $f(z)$ be an analytic function defined on W^- satisfying $\mathrm{Im} f(z) \to 0$ as $z \to W \cap \mathbb{R}$. Then, $f(z)$ extends to be analytic on W such that*

$$f(\bar{z}) = \overline{f(z)} \tag{2}$$

We now illustrate how the Schwarz reflection principle applies to conformal maps of sectors of the complex plane. Consider a circular sector occupying $\pi/4$ rad of the interior of the unit circle, which we denote $W^-_{\pi/4}$, as depicted in Fig. 2(*a*). The Riemann mapping theorem guarantees that this sector can be transformed into any other simply-connected region by a conformal map. In particular, the mapping theorem ensures that there exists a mapping function $f(z)$ to the region Ω_- depicted on the right side of Fig. 2(*a*), whose boundary we denote as Γ. Figure 2(*a*) illustrates just one particular choice of Ω_-. If Ω_- is taken instead to be the shaded element in Fig. 3(*b*), the shape obtained by Schwarz reflections in Fig. 2(*d*) becomes a regular pentagon. A large class of shapes can be obtained through Schwarz reflections of various choices of Ω_-, a few of which are illustrated in Fig. 4.

Our analysis applies generally to situations where the boundary curve Γ has the following properties. Consider a wedge sector of the complex plane spanning some angle, with its boundaries defined by two straight lines emanating from the origin. Now choose one point on each sector boundary and call the straight segments from the origin to each of these two points L_1 and L_2. Now connect the open endpoints of L_1 and L_2 to one another with a nonself-intersecting curve γ which only intersects the sector boundaries at its endpoints. We call the outer curve, γ, a *primitive edge*. Then, we define the *primitive curve*, $\Gamma \equiv L_1 \cup L_2 \cup \gamma$. We call the shape bounded by Γ, int(Γ), the *primitive shape*. Primitive shapes are shaded in all figures herein.

In addition, we can choose the image location of three pre-image points under the mapping $f(z)$, all of which are labeled as black circles in Fig. 2(*b*). Then, $f(z)$ maps the domain $W^-_{\pi/4}$ onto its image Ω_- and maps the three pre-image points to the three image points.

Now consider the region $W = W^+_{\pi/4} \cup W^-_{\pi/4}$, in the pre-image domain, which is symmetric about the real axis and illustrated on the left of Fig. 2(*b*). It is clear that W meets the criterion of the Schwarz reflection principle, and so it is guaranteed that the domain of analyticity of $f(z)$ may be extended from $W^-_{\pi/4}$ to W. Moreover, it is guaranteed that the analytic extension of $f(z)$ defined over W satisfies Eq. (2). It is thus clear that the image of W, under the analytic extension of $f(z)$, is $\Omega = \Omega_- \cup \Omega_+$, as drawn on the right of Fig. 2(*b*).

To extend the mapping domain further, we first rotate the pre-image W from Fig. 2(*b*) about the origin by $\pi/4$ rad clockwise: specifically, the new map is written in terms of the old as $\exp(-i\pi/4) f(\exp(i\pi/4)z)$. We next apply the Schwarz reflection principle about the real axis—again taking W_- to be a sector of $\pi/4$ rad in the unit circle (below the real axis) and Ω_- to be one primitive sector below the real axis—from which we obtain the extended map

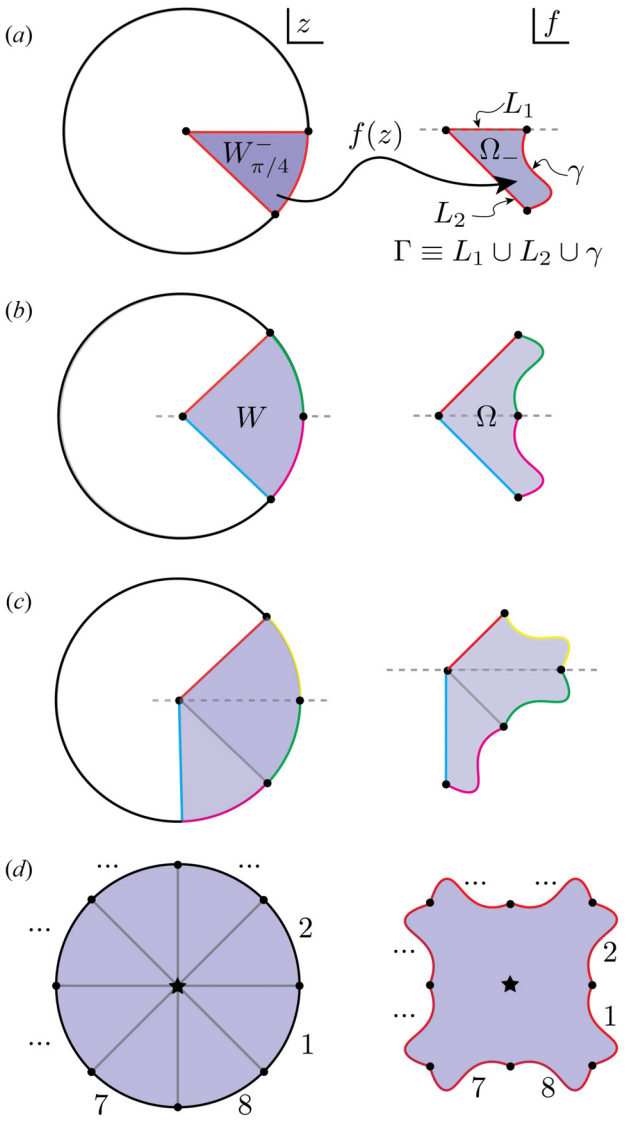

Fig. 2 Demonstration of the sector reflection principle of Hersch [7]. The Riemann mapping theorem guarantees the existence of an analytic mapping $f(z)$ between $W^-_{\pi/4}$ and Ω_- as indicated in panel (*a*). The Schwarz reflection principle guarantees $f(z)$ may be analytically extended to W with the boundary correspondence as indicated in panel (*b*). Rotating clockwise by $\pi/4$ and reflecting again leads to panel (*c*). By performing rotations and reflections, the domain of analyticity of $f(z)$ may be extended to the entire unit circle. The image and boundary correspondence of the mapping from the unit circle is given in panel (*d*).

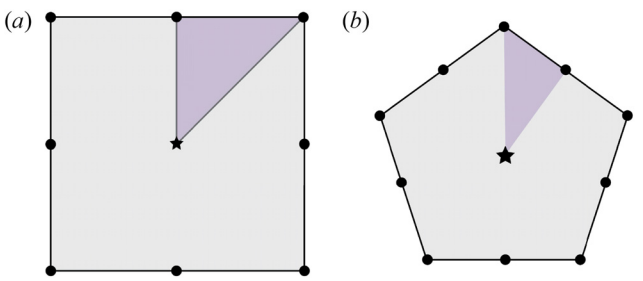

Fig. 3 Example primitive sectors for the (*a*) square ($N = 8$) and (*b*) pentagon ($N = 10$) are shaded. The conformal map from the interior of the unit disk to the square maps each wedge spanning $2\pi/N$ to each of the primitive shapes in Fig. 3.

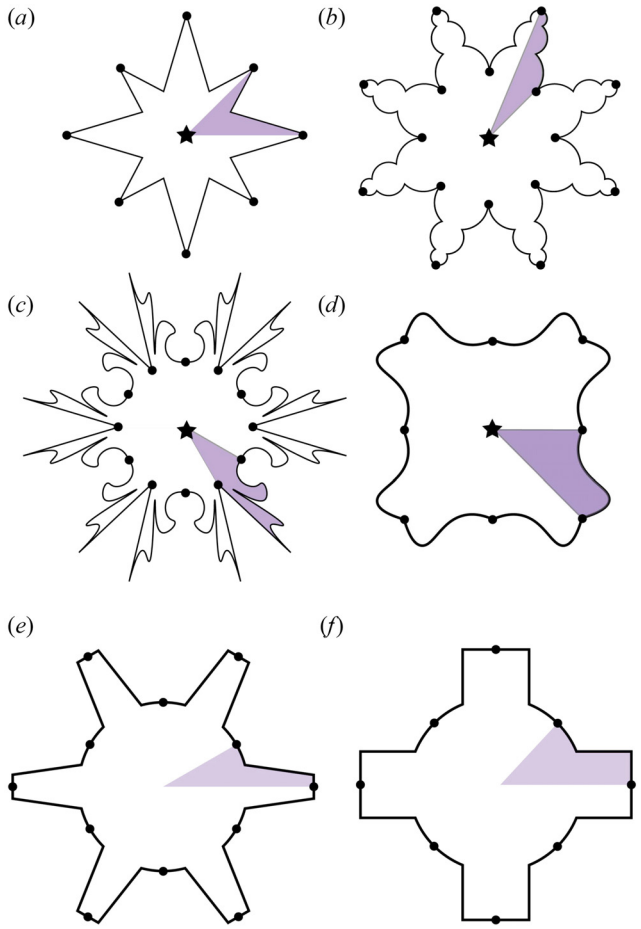

Fig. 4 Example of some irregular shapes that may be constructed from sector reflections of a primitive shape (shaded) for cases of (*a*) $N = 8$, (*b*) $N = 16$, (*c*) $N = 12$, (*d*) $N = 8$, (*e*) $N = 12$, and (*f*) $N = 8$. Panels (*e*) and (*f*) demonstrate that gearlike configurations satisfy the conditions of Theorem 2.

illustrated in Fig. 2(*c*). At this point, we have constructed a map that takes a wedge spanning $3\pi/4$ rad in the unit circle to an object containing three primitive shapes (see Fig. 2(*c*)).

Repeating the procedure of a rotation followed by a sector reflection, one may achieve a mapping of the full unit circle onto the shape in the right panel of Fig. 2(*d*). Generally, if a body is composed of N primitive shapes, one must perform $N-1$ sector reflections of the primitive shape to construct a map from the unit circle. For example, a total of seven reflections are used to generate the map in Fig. 2(*d*). Note the geometric requirement that N be even.

In Fig. 2(*d*), the equal length boundary segments labeled 1–8 on the unit circle boundary are mapped by $f(z)$ to the corresponding labeled segments in the right panel. Despite the fact that the Riemann mapping theorem generally only guarantees three degrees-of-freedom in a conformal map, symmetry has allowed us to fix the location of *nine* points: eight boundary points and the origin in Fig. 2(*d*).

More generally, if a Jordan curve ∂B may be constructed from N sector reflections of a primitive edge, then there exists a conformal map from the interior of the unit circle to $B \equiv \text{int}(\partial B)$ which maps each of N equal length arcs on the unit circle to a primitive edge in ∂B.

It follows that if boundary conditions are specified (and unchanging) along each of the N primitive edges in ∂B, then the shape factor problem in B is conformally equivalent to the problem interior to the unit circle having the same boundary conditions specified on N arcs of equal length. The conformal transformation between the two domains is given by $f(z)$ as constructed in Fig. 2(*d*).

We now move to consideration of the boundary value problem on the exterior region to B, $\mathbb{C}\,B$, satisfying the same boundary conditions on ∂B. We proceed to show the conformal equivalence between the interior and exterior boundary value problems under the following assumptions: (1) B may be constructed by sector reflections of a primitive shape and (2) the boundary conditions on ∂B do not change along any primitive edge.

3.2 The Exterior Problem: Shapes Built From Sector Reflections Have $S_i = S_e$. Consider again a Jordan curve ∂B which may be constructed by $N-1$ sector reflections of a primitive edge. For illustration, let this be the same boundary curve ∂B as considered in Sec. 3.1 (Fig. 2(*d*)). We now examine the heat transfer problem exterior to that curve, in the region $\text{ext}(\partial B)$, which is shaded on the right of Fig. 5(*c*). Since the shape factor is invariant under conformal mapping, we may establish the equality of the interior and exterior shape factors, relative to the curve ∂B, by showing that both the exterior and interior problems can be mapped onto the same problem on the interior of the unit disk (illustrated in Fig. 2(*d*)). We now proceed to demonstrate this fact.

We now construct the conformal map from the unit circle interior to $\text{ext}(\partial B)$, as outlined in Fig. 5. First, consider the curve labeled $1/\Gamma$ on the right of Fig. 5(*a*). This curve is constructed by transforming each point in the primitive curve Γ, from Fig. 2(*a*), according to the mapping $z \to 1/z$; the resultant primitive curve is denoted $1/\Gamma$. By applying the arguments of Sec. 3.1 to this new primitive curve, one can construct a mapping $g(z)$ from the unit circle interior to the interior of the shape in the right side of Fig. 5(*b*), which is itself constructed through sector reflections of $1/\Gamma$. The boundary

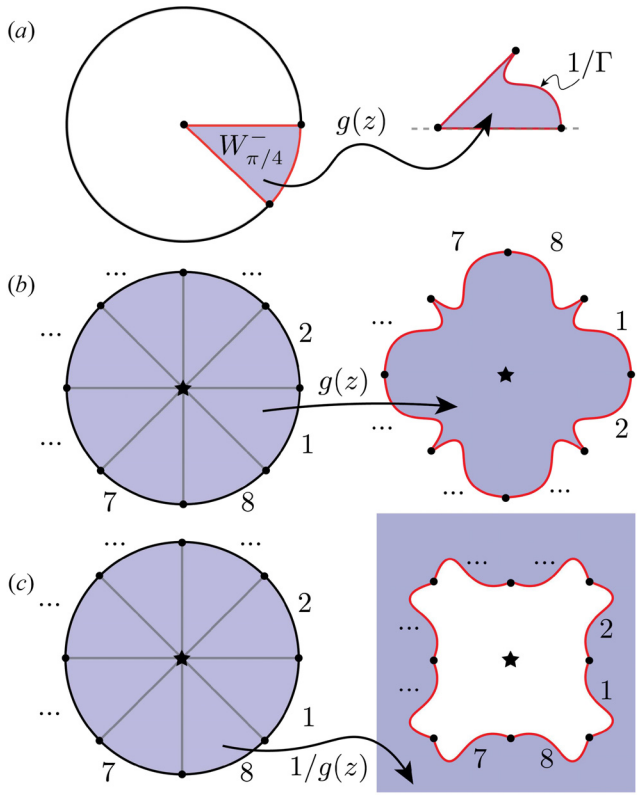

Fig. 5 Construction of the map between the unit circle interior and the exterior problem, using sector reflections. The Riemann mapping theorem guarantees a mapping $g(z)$ between $W^-_{\pi/4}$ and the region enclosed by $1/\Gamma$, as depicted in (*a*). By applying sector reflections (as was done in Fig. 2) the domain of analyticity of $g(z)$ is extended to the entire unit disk as illustrated in panel (*b*). Note that the map in panel (*b*) is to an entirely new shape. The map $1/g(z)$ then sends the interior of the unit circle to exterior domain of interest.

correspondence under the mapping $g(z)$ is labeled. Note that the boundary correspondence in Fig. 5(*b*) is now clockwise (compared to counterclockwise in Fig. 2(*d*)) because here the Schwarz reflection principle was applied to the sector $1/\Gamma$ in Fig. 5(*a*) which was *above* the real axis. In a final step, the reciprocal map $1/g(z)$ sends the interior of the unit circle to $\text{ext}(\partial B)$, as illustrated in Fig. 5(*c*). The boundary correspondence is labeled, the reciprocal map having reinstated the clockwise order.

As before, if boundary conditions are unchanging over each primitive edge, the exterior shape factor problem is conformally equivalent to the problem interior to the unit circle having the same boundary conditions on equiangular arcs. Figures 2(*d*) and 5(*c*) thus reveal that, under the same boundary conditions on ∂B, the interior and exterior shape factor problems may both be mapped to the same problem on the unit circle interior. Thus, the interior and exterior shape factor problems are conformally equivalent and possess the same shape factor and $S_e = S_i$.

Note that one may apply similar arguments to construct a mapping directly between the interior and exterior problems. However, we find it instructive to introduce the auxiliary problem on the unit circle interior and to show the conformal equivalence there. It should be clear to the reader that the map $1/g(f^{-1}(z))$ directly maps the interior problem (right side of Fig. 2(*d*)) to exterior problem (right side of Fig. 5(*c*)) while preserving the locations of the primitive boundary segments.

3.3 A Precise Statement of the Theorem. The preceding Secs. 3.1 and 3.2, outline a set of criteria whose fulfillment implies the equality of interior and exterior shape factors. At this stage, the more mathematical reader will beg the authors to state these criteria concisely in the form of a theorem. Consider first a definition.

Consider a partition of the complex plane, $\mathbb{C}$, into some positive whole number, N, of equiangular wedge sectors centered on the origin. For example, the case of $N = 8$ is depicted in the left of Fig. 2(*d*), provided each gray line extends to complex infinity ($|z| \to \infty$). We call this arrangement an *N-sector partition* of the complex plane.

THEOREM 2 (Interior/Exterior Shape Factor Equality). *Consider an N-sector partition of the complex plane, for an even value $N \geq 4$. Now consider a Jordan curve ∂B constructed from $N-1$ sector reflections of a primitive edge. Suppose that each primitive edge of ∂B is subjected to either a zero Neumann (adiabatic) or a constant Dirichlet (isothermal) boundary condition, with the Dirichlet constant restricted to one of two temperatures. Additionally, Dirichlet sections at different temperatures must be separated by at least one adiabatic section. Then, the shape factors for heat transfer in the domains* $\text{int}(\partial B)$ *and* $\text{ext}(\partial B)$ *are equal.*

Note that we require N to be greater or equal to four because the boundary conditions may not change along any primitive edge. Since the simplest heat transfer problem having a finite shape factor comprises two isothermal segments separated by two adiabatic segments, a minimum of $N = 4$ is required to specify all four segments in accordance with the boundary condition criterion.

4 The Unit Disk, Regular *K*-Gons, and Beyond

We now explain, using the theoretical tools developed in Secs. 3.1 and 3.2, why the boundary value problems analyzed by Lienhard [8] happened to have $S_i = S_e$. We shall show that all cases considered therein were within the scope of Theorem 2. We also discuss more general shapes and Yin–Yang bodies.

4.1 The Counterexample of the Rectangle. We now describe how the rectangle violates the assumptions laid out in Theorem 2. Any rectangle may be constructed from successive reflections of a smaller interior similar rectangle (the primitive shape) as depicted in Fig. 6(*a*). Theorem 2 thus guarantees the equality of interior and exterior shape factors if boundary conditions are specified along the associated primitive edge, as illustrated in Fig. 6(*b*). For the rectangle shown in Fig. 1(*a*), however, each boundary conditions is specified along portions of two primitive edges (e.g., the entire top), and so Theorem 2 is not applicable.

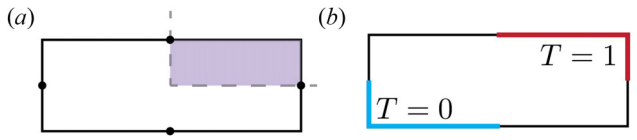

Fig. 6 (*a*) The rectangle can be constructed by successive reflections of a smaller primitive rectangle (shaded), and $N = 4$ and (*b*) an example shape factor problem where $S_i = S_e$ is guaranteed by Theorem 2

4.2 The Square. The square interior domain comprises eight of the primitive triangles shaded in Fig. 3(*a*). It follows from the developments of Secs. 3.1 and 3.2 that the mapping from the square's interior to its exterior will preserve the eight primitive edges (segments connecting each pair of adjacent black circles in Fig. 3(*a*)). Lienhard [8] numerically tested two configurations of boundary conditions on the square. Both examples considered therein specified boundary conditions unchanging along each primitive edge, in accordance with the assumptions of Theorem 2, and it was indeed found that $S_i = S_e$.

Nonetheless, the equality of interior and exterior shape factors does not generalize to arbitrary problems. Symmetries of both the domain boundary shape and the boundary condition specification are required to guarantee the equality of interior and exterior shape factors: (1) the shape interior $\text{int}(\partial B)$ must be constructable from sector reflections of a primitive shape; and (2) boundary conditions must be unchanging along each primitive edge.

4.3 Regular *K*-Gons. A regular K-gon can be constructed from $N = 2K$ copies of a primitive triangle; we illustrate the primitive triangles for the cases $K = 4$ and $K = 5$ in Fig. 3. If only one boundary condition is specified as unchanging along each primitive edge, then the interior and exterior shape factors are guaranteed to be equal, in accordance with Theorem 2.

Specifically for regular K-gons, primitive edges are half-faces. Thus, a single boundary condition must be specified along the entirety of each half-face to ensure that $S_i = S_e$. For example, the square of Sec. 4.2 has $K = 4$, but boundary conditions are allowed to vary between its $N = 2K = 8$ primitive edges (half-faces), for Theorem 2 to be applicable and thus to ensure the equality of interior and exterior shape factors.

To validate this somewhat surprising result, we use finite element method (FEM) to compute the interior and exterior shape factor of the hexagon with half-heated faces in the last row of Table 1. Here, the top and bottom faces of the hexagon have opposite halves at different temperatures, while the remainder of the hexagon boundary is taken to be adiabatic. The computed interior and exterior shape factors are shown together with the analytical result for the interior problem given by Hersch [6], $S_i = 1/\sqrt{3}$. The interior value is within 0.03% of the exact result, and the exterior value is within 1.3%. While the exact solution $S_i = 1/\sqrt{3}$ given by Hersch was computed for the interior problem, Theorem 2 indicates the same exact result for the exterior problem, as is supported by our numerical calculations.

4.4 The Disk. For the disk, the map $1/z$ takes the interior problem to the exterior problem with the same boundary conditions (up to a reflection, which does not affect the shape factor). Thus, for any alternating sequence of constant Dirichlet and Neumann conditions around the boundary of a circle, the interior and exterior problems are conformally equivalent and $S_i = S_e$ must hold.

In light of Sec. 4.3, one may also rationalize the equality of the interior and exterior shape factors of the circle in the following manner. Consider the circle as the limit of a regular K-gon, whose vertices lie on the unit circle, as $K \to \infty$. For the K-gon, the interior

Table 1 Shape factors for selected K-gons, comparing known exact values to interior and exterior FEM results. Interior and exterior flux plots are shown, except for second and third exterior cases which show temperature field. Thick lines are isothermal boundaries. The fifth case satisfies $N = 2K = 12$ as discussed in Sec. 4.1, with boundary conditions specified on half sides.

N	Interior	S_i (FEM)	S_{exact}	S_e (FEM)	Exterior
8	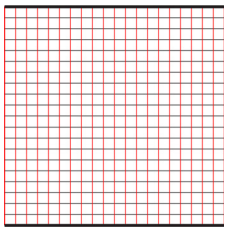	1.0000	1	0.9948	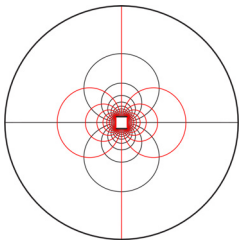
12	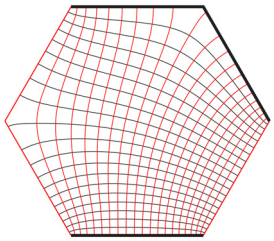	0.9998	1	0.9882	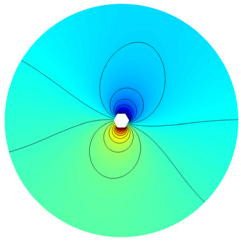
12	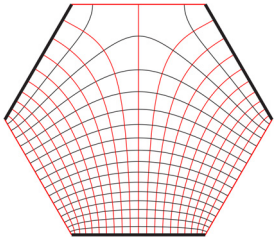	1.1544	$1.15470\cdots$ $(2/\sqrt{3})$	1.1427	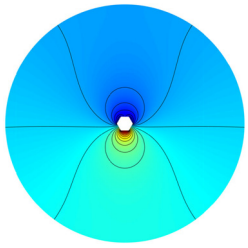
16	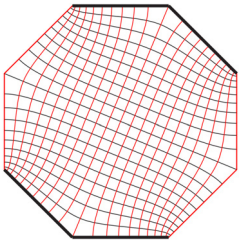	0.9994	1	0.9896	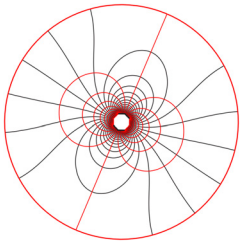
12	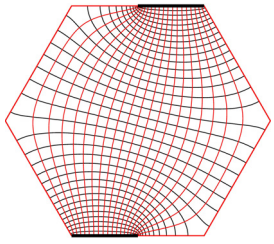	0.5776	$0.57735\cdots$ $(1/\sqrt{3})$	0.5700	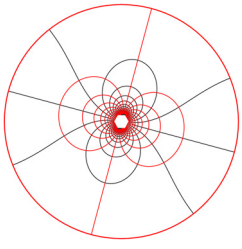

Far-field boundary conditions for the exterior are: square—dipole temperature field with radius 20; hexagon—adiabatic outer boundary with radius 30; and octagon—adiabatic outer boundary with radius 35. Each polygon has sides of length 2.

and exterior shape factors are guaranteed to be equal as long as boundary conditions are constant along each of the $2K$ primitive edges. In the limit of $K \to \infty$, the length of each primitive edge tends to zero. In this limit, any finite segment of the circle can be decomposed into a union of primitive segments. Thus, for any shape factor problem on the circle, with finite boundary segments possessing different boundary conditions, it is guaranteed that $S_e = S_i$.

4.5 Other Shapes. Note that our criteria, which guaranteed $S_i = S_e$, do not require shapes to be regular polygons—or any other simple shape for that matter. The first criterion (geometric criterion) is that the domain may be constructed from sector reflections of a primitive curve confined to a sector of angle $2\pi/N$ with $N \geq 4$ being some even integer. Some examples of more complex objects are given in Fig. 4, with primitive shapes shaded. Note that for Theorem 2 to apply, ensuring the equality of interior and exterior shape factors, applied boundary conditions must be unchanging along each primitive edge.

4.6 Yin–Yang Bodies Have $S_i = S_e = 1$. We here demonstrate how Schwarz reflections may be used to prove another interesting symmetry of shape factors, the Yin–Yang property [10], which is outlined as follows.

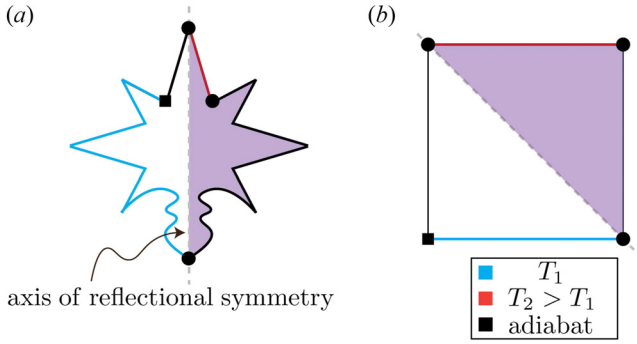

Fig. 7 Conformal equivalence of Yin–Yangs and the square problem with $S = 1$. The domain in panel (*a*) embodies the Yin–Yang symmetry as described in Sec. 4.6. By the Riemann mapping theorem, there exists a mapping between the shaded section of the domain in (*a*) and the half-square with the drawn boundary correspondence as drawn in panel (*b*). The Schwarz reflection principle then gives the remainder of the map (white region with the illustrated boundary correspondence). Since the shape factor of (*b*) is trivially equal to unity, by the conformal invariance of the shape factor, $S = 1$ in (*a*) as well.

Suppose a Jordan curve ∂B has an axis of reflectional symmetry, as shown in Fig. 7. The boundary on one side of the axis contains an isothermal segment and an adiabatic segment; on the reflected side, the isothermal and adiabatic conditions have been interchanged. When a shape factor problem embodies all the aforementioned symmetries, we say it embodies the Yin–Yang symmetry. Lienhard [10] stated that Yin–Yang problems have a shape factor of unity, although no formal proof was given.

Here, we use Schwarz reflections to provide a proof that all such shape factor problems are conformally equivalent to a problem on the square which possesses $S = 1$. Consider a shape factor problem embodying the Yin–Yang symmetry as in Fig. 7(*a*). Now consider single half of the domain (shaded), as defined by a cut made along the axis of symmetry (gray dotted line). By the Riemann mapping theorem, there exists a mapping between the shaded region in Fig. 7(*a*) and the shaded half of the square (Fig. 7(*b*)), wherein we are free to dictate the image location of three boundary points. In particular, we choose to specify the images of the three following boundary points (shown with black circles): the two intersections of ∂B with the reflection axis, and the point where the isothermal boundary segment adjoins the adiabatic boundary segment. We choose as the images of these three points the three vertices of the square also indicated by black circles. The boundary condition correspondence is colored in both panels. The Schwarz reflection principle then implies the image of the remainder of the domain (white region), for which the boundary correspondence is also indicated in Fig. 7. Since the shape factor of Fig. 7(*b*) is trivially $S = 1$, the conformal invariance of the shape factor shows that $S = 1$ in Fig. 7(*a*) as well.

By a similar argument to Sec. 3.2, the proof also holds for the exterior Yin–Yang problem, so that the interior and exterior Yin–Yang shape factor problems must have $S_i = S_e = 1$.

Finally, we note that the Yin–Yang problem shows that, although our criteria in Theorem 2 are sufficient to guarantee $S_i = S_e$, they are not necessary criteria: many Yin–Yangs do not meet the criteria of Theorem 2, but all have equality of their interior and exterior shape factors.

5 Validation for Several Cases

We now show several explicit results to support our conclusion.

5.1 Interior and Exterior Numerical Results Compared to Exact Shape Factors. Table 1 contains several cases for which exact interior shape factors are known. Interior and exterior simulations are shown, along with the computed shape factors. The interior FEM results are accurate to 0.05% or better (see Appendix A). The exterior FEM results are accurate to about 1.5%, with most of the error attributable to a finite outer domain. In all cases, the exact, interior, and exterior results agree to within the apparent accuracy of the FEM computations. Additional numerically validated K-gons are shown in Appendix D.

Note that in the third row in Table 1 the two upper segments have the same temperature, but are not connected. Theorem 2 applies to such cases without limitation.

The exact values for the first, second, and fourth cases in Table 1, $S = 1$, arise because these problems have Yin–Yang symmetry (Sec. 4.6). The exact results for third and fifth cases were found by Hersch for the interior geometries [6]. We have proven herein that Hersch's exact values for the interior domain are also those for the exterior problem. Thus, we label these exact results S_{exact} since there is distinction between the interior and exterior shape factors. Our numerical results support our proof.

5.2 The Compass Rose. The compass rose is a design traditionally used to display the cardinal directions on a map, consisting of four orthogonal arms of one length and four of another at a 45 deg rotation. In the language of this paper, the compass rose has an $N = 8$ symmetry with a primitive element containing one-half arm of each length (Fig. 3(*a*)).

To further demonstrate the applicability of our theorem, we have simulated heat conduction inside and outside the rose for two arrangements of boundary conditions compatible with Theorem 2 (see Table 2). The first case specifies isothermal boundary conditions on four identical sections of the boundary, with edges in the upper right-hand and lower left-hand quadrants at different temperatures. This case embodies the Yin–Yang symmetry so that $S_{\text{exact}} = 1$.

The second case has isothermal boundary conditions specified in an asymmetric fashion. The two primitive elements in the upper right-hand quadrant have edges at one temperature, and one primitive element in the lower right-hand quadrant a different temperature. (The theoretical value for this case is given in Sec. 6.)

The numerical value of S_i for the first case is within 0.12% of the theoretical value. The numerical value of S_e is 2.6% below the theoretical value, primarily owing to the difficultly in capturing the very strong singularities of the heat flux at the tips of the long arms. A further difficulty with this, and other, exterior computations is the need to truncate the infinite domain with an outer boundary of sufficient size (see Appendix A.2). If nothing else, these difficulties illustrate the great value in knowing that S_e can be found through the much easier computation of S_i. The interior agreement is similar for second case, with the outside value lower than the theoretical value by 3.5%.

5.3 Known Conformal Maps for *K*-Gons. The explicit Schwarz–Christoffel transformations between the unit circle and the K-gon interior and exterior show that the interior and exterior problems are conformally equivalent when each K-gon face adopts a single boundary condition [11]. These transforms are discussed briefly in Appendix B. While the Schwarz–Christoffel maps show that $S_e = S_i$ when boundary conditions do not vary over each full face, our results in Sec. 3.2 indicate a less restrictive requirement: boundary conditions must not vary over each *half*-face.

6 An Analytic Expression for Shape Factors With *N*-Fold Symmetry

We now present an expression for the shape factor for a *quadrilateral*—a shape with four distinct boundary sections—that has an N-fold symmetry. Consider a polygon with N sides. Begin with the hot isothermal segment of the boundary, and suppose this extends over N_H sides of the polygon. Next, proceeding clockwise around the polygon, suppose the length of the adjacent adiabatic section is N_A. Proceeding clockwise again, suppose the adjacent the cold isothermal section spans N_C sides. Then, the remaining

Table 2 Shape factors for the compass rose. Temperature field and isotherms are shown.

N	Interior	S_i (FEM)	S_{exact}	S_e (FEM)	Exterior (near field)
4	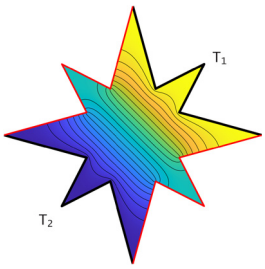	0.9988	1	0.9740	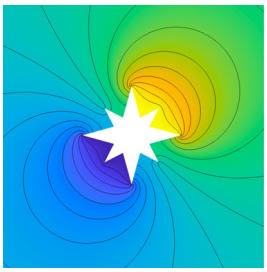
8	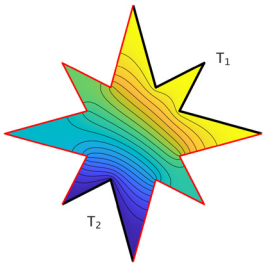	0.8187	0.819644 $\cdots$	0.7907	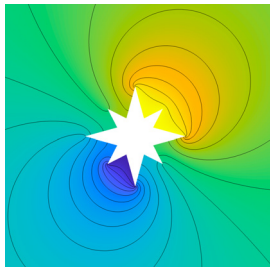

The far-field boundary is adiabatic with radius 30. The long arms have a radial length of 1.5, the short arms have 1.17, and the inner vertices have 0.6.

Table 3 Interior flux plots for all unique regular pentagons and hexagons, with exact shape factors obtained through Eq. (3) along with numerical values from FEM. Isothermal sides are shown with thick lines. Isotherms and adiabats are shown with thin lines.

Case		S_{exact}	S_i (FEM)	Case		S_{exact}	S_i (FEM)
S_p^{1-1}	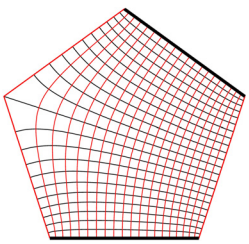	0.896256	0.8963	S_p^{2-1}	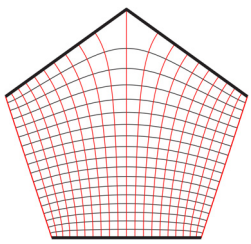	1.11575	1.1157
S_h^{1-1}	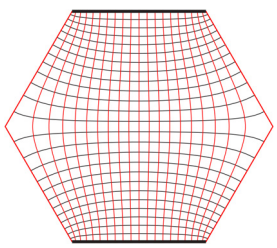	0.781701	0.7815	S_h^{1-1R}	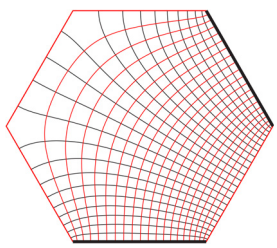	0.854584	0.8544
S_h^{2-1}	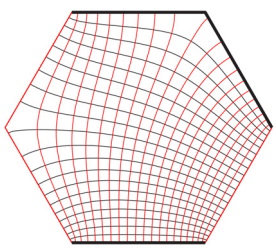	1	0.9998	S_h^{3-1}	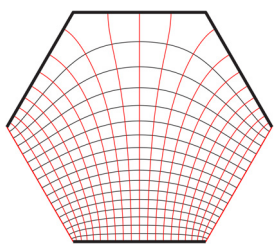	1.17016	1.1699
S_h^{2n-1}	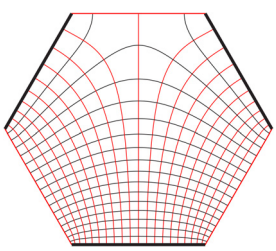	$2/\sqrt{3}$ (1.15470 $\cdots$)	1.1544	S_h^{2-2}	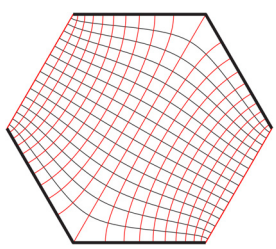	1.27926	1.2790

Table 4 Flux plots and shape factors for squares with two isothermal half-sides. The half-side at T_1 is the bottom right. The half-side at T_2 is: UL—upper left; TL—top left; TR—top right; and UR—upper right. Exact values are from Eqs. (3) and (7).

Case		S_{exact}	S_i (FEM)
UL	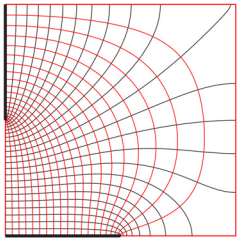	$0.819644\cdots$	0.8197
TL	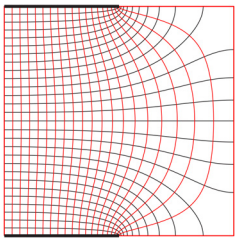	$1/\sqrt{2}\ (0.707106\cdots)$	0.7073
TR	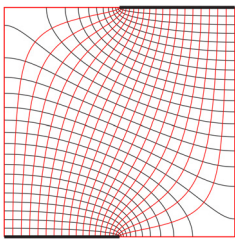	$0.680634\cdots$	0.6808
UR	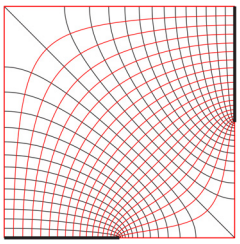	$1/\sqrt{2}\ (0.707106\cdots)$	0.7073

adiabatic side spans $N-(N_H+N_A+N_C)$ polygon sides. In this case, the shape factor is given by

$$S(N_H,N_A,N_C,N)=\frac{K\left(\sqrt{1-C^2}\right)}{K(C)} \tag{3}$$

$$C(N_H,N_A,N_C,N)=\sqrt{\frac{\sin\left(\frac{N_A\pi}{N}\right)\sin\left(\frac{(N_A+N_C+N_H)\pi}{N}\right)}{\sin\left(\frac{(N_A+N_C)\pi}{N}\right)\sin\left(\frac{(N_A+N_H)\pi}{N}\right)}} \tag{4}$$

$$K(x)=\int_0^1\frac{dk}{\sqrt{1-k^2}\sqrt{1-k^2x^2}} \tag{5}$$

Note that the definition of the elliptic function in Eq. (5) varies between authors; for example, the elliptic function in MATHEMATICA, K_{MA}, is related to our definition by $K(x)=K_{\text{MA}}(x^2)$. In the context of Laplace problems, we find the definition presented in Eq. (5) to be most common. This formula is proved in Appendix C.

To demonstrate the utility of our formula, we now compute the shape factors for several nontrivial problems; the values are verified numerically using FEM analysis in Appendix D. For example, the first pentagon in Table 3 has $N=5$, $N_H=1$, $N_A=2$, and $N_C=1$, in which case our formula gives $S(1,2,1,5)=0.896256$, which agrees with the FEM calculation to 0.005%. As another example, the last hexagon in Table 3 has $S(2,1,2,6)=1.27926$, within 0.02% of the numerical result. The compass rose problem illustrated in the bottom row of Table 2 has $N=8$, $N_H=1$, $N_A=3$, and $N_C=2$, and our formula (3) returns $S(1,3,2,8)=0.819644\cdots$, within 0.12% of the numerical value in Table 2. The compass rose has many exterior corner singularities which are hard to resolve with FEM, as was noted in Sec. 5.2, emphasizing the utility of Eq. (2).

As a final demonstration of the power of Eq. (3), we note that the elliptic integral can be evaluated exactly is certain cases. In the half-square geometry TL in Table 4, the shape factor is given by $S(1,2,1,8)$. With Eq. (4)

$$C(1,2,1,8)=\frac{\csc(3\pi/8)}{2^{1/4}}=\frac{2^{3/4}}{\sqrt{2+\sqrt{2}}} \tag{6}$$

Letting $K'(x)=K(\sqrt{1-x^2})$, we make use of the relation [12] $K'(x)/K(x)=(1/2)K'(\eta)/K(\eta)$, where $\eta(x)=(1-\sqrt{1-x^2})/(1+\sqrt{1-x^2})$. Applying this identity to Eq. (3), with argument $C(1,2,1,8)$ as given in Eq. (6), we find $\eta(C(1,2,1,8))=\sqrt{2}-1$ and

$$S(1,2,1,8)=\frac{1}{2}\frac{K'\left(\sqrt{2}-1\right)}{K\left(\sqrt{2}-1\right)}=\frac{1}{\sqrt{2}} \tag{7}$$

where we have used $K'(\sqrt{2}-1)/K(\sqrt{2}-1)=\sqrt{2}$ [12]. Since $1/\sqrt{2}=0.707107\cdots$, the numerical result in Table 4 agrees with the analytical result to within 0.03%.

The new analytical solution, Eq. (3), is not restricted to polygons or star shapes. As long as a body has an N-fold symmetry, and the quadrilateral boundary conditions are specified along full entire segments of the primitive element, Eq. (3) is valid. For example, consider the puffy snowflake in Fig. 4(*b*). The shape has 16 primitive edges. Suppose one edge is set to T_1. Then, proceeding clockwise, let the next five primitive edges be adiabatic. Continuing clockwise, let the next four primitive edges be isothermal at T_2, with the remainder adiabatic. The shape factor is then $S(1,5,4,16)=0.6869\cdots$. One may proceed similarly to find the shape factor in a wide variety of problems including all of those in Fig. 4.

Our analytical solution holds whenever shapes have an appropriate symmetry, but it does not rely on the specific details of the primitive elements. Thus, in even very complicated geometries that are extremely difficult to tackle numerically (for example, Fig. 4(*c*)), Eq. (3) holds. The formula may thus be used as a benchmark for numerical methods meant to deal with such extreme geometries [13]. Further, as a result of Theorem 2, Eq. (3) yields the shape factor exterior to such complex shapes, for which numerical solutions would be very challenging to obtain.

7 Analogues in Darcy Flows and Electrostatic Capacitance

The results presented in Sec. 3 have precise mathematical analogues in fluid flow through porous media and in electrical capacitance, which we now briefly outline.

7.1 Darcy Flow Through Porous Media. Pressure-driven flow through a porous media has a velocity given by $\mathbf{u}=-\sigma\nabla P$, where σ is the hydraulic conductivity, and P is the pressure. Mass conservation for an incompressible fluid then implies that the pressure satisfies the Laplace equation. Consider a situation where flow is driven between isobaric segments held at two different pressures, and separated by impermeable segments, with a pressure difference ΔP. Then, the volume flux between the isobaric

segments, Q_f, can be written in terms of a flow shape factor S_f which depends on the geometry according to

$$Q_f = S_f \sigma \Delta P \tag{8}$$

The present results apply to flow through a porous media after the following modifications: k is replaced by the hydraulic conductivity σ; ΔT is replaced by the pressure differential between isobaric segments ΔP; the heat flux Q is replaced by the volume flux Q_f; and the shape factor is replaced a flow shape factor S_f. Note also that in the fluid flow context, thermal conductors and insulators are replaced by isobaric segments and impermeable boundaries, respectively. In the fluid flow context, Theorem 2 guarantees the equivalence of the flow shape factors interior and exterior to a body.

7.2 Electrostatic Capacitance. When a voltage differential is established between two perfect electrical conductors, a charge of magnitude q is established on each conductor. For a given voltage differential ΔV, the amount of charge q is characterized by the electrostatic capacitance C, which is a function of the geometry, according to

$$q = C \Delta V \tag{9}$$

Our results apply to the electrical capacitance, C, after the following substitutions: ΔT is replaced by electrical potential difference between conducting segments ΔV; Q/k is replaced by the conductor surface charge q; and the shape factor is replaced by the electrical capacitance C. Thermal conductors and insulators must be replaced by electrical conductors and insulators, respectively. Theorem 2 guarantees the equivalence of the electrostatic capacitances interior and exterior to a body.

8 Summary

Interior and exterior shape factors are not universally equal, contrary to a previous report. In this paper, we first demonstrated why the interior and exterior shape factors are not always equal. We then provided a set of criteria sufficient to guarantee equality. In particular, the interior and exterior shape factors *will be equal* if specific symmetries are present: (1) the shape boundary must be constructed from sector reflections of a primitive sector edge; and (2) the boundary conditions—either zero Neumann (adiabatic) or constant Dirichlet (isothermal)—must not change along each primitive edge. This result is stated precisely in Theorem 2.

Objects that meet the conditions of the theorem include not only regular polygons and disks but also much more complex shapes like those shown in Fig. 4. These results have direct analogies in flow through porous media and in electrostatic capacitance, as outlined in Sec. 7.

We have further derived an exact expression for the shape factor of appropriately symmetric N-sided objects that have contiguous sides at one temperature separated from contiguous sides at another temperature by one or more adiabatic sides. This expression, Eq. (3), applies not only to regular polygons and star shapes but also to any other shape that has N-fold symmetry. We have validated this powerful result with FEM analysis of multiple configurations.

We have tested our theorem against independent results from finite element simulations and from Schwarz–Christoffel maps. Additionally, a brief tabulation of shape factors in geometries that meet the conditions of Theorem 2 is provided in Appendix D.

We note that this paper may be useful also as an accessible tutorial for applying symmetry methods to Laplace problems through the exploitation of the Schwarz reflection principle.

Acknowledgment

K.M. would like to thank Alex Cohen and Darren Crowdy for valuable discussions. Both authors would like to thank Nick Trefethen for useful comments and for pointing out the work of Hersch.

Funding Data

- Massachusetts Institute of Technology (MathWorks Fellowship; Funder ID: 10.13039/100006919).
- STEM Chateaubriand Fellowship, Ambassade de France aux États-Unis

Data Availability Statement

The authors attest that all data for this study are included in the paper.

Nomenclature

a, b = dimensions of rectangle
B = a planar body (interior of a Jordan curve, ∂B)
b_k = prevertices on unit disk
$\mathbb{C}$ = the set of complex numbers
c_1, c_2, c_3 = constants, Appendix B
CR = cross-ratio, Eq. (C3)
$C(N_H, N_A, N_C, N)$ = see Eq. (4)
ext(∂B) = region exterior to ∂B
$f(z), g(z)$ = conformal maps
$H_{\max}$ = maximum mesh size for FEM
int(∂B) = region interior to ∂B
k = thermal conductivity (W m^{-1} K^{-1})
K = number of sides in polygon
$K(x)$ = complete elliptic integral of the first kind, Eq. (5)
$K'(x)$ = complementary elliptic integral, $K(\sqrt{1-x^2})$
L_1, L_2 = straight lines along each sector boundary extending from the origin to the ends of the primitive edge, Fig. 2(*a*)
N = number of primitive elements composing a shape
N_A, N_C, N_H = number of contiguous adiabatic, cold, and hot sides
Q = heat flow (W m^{-1})
S = shape factor (-)
$S(N_H, N_A, N_C, N)$ = see Eq. (3)
T = temperature (K)
W = domain in the complex z plane
x = coordinate along the bottom wall, Appendix A.1
z = coordinate in the complex plane

Greek Symbols

α = angle on disk, see Fig. 8
γ = outer section of boundary denoted a primitive edge, Fig. 2(*a*)
Γ = closed curve defined by $\Gamma = L_1 \cup L_2 \cup \gamma$, and denoted the primitive curve
$\delta x = H_{\max}/2$
ΔT = temperature difference (K)
$\eta_1 = K/[2(K+2)]$
μ_i = exterior angles as fraction of π
Ω = range in the mapped plane

Superscripts and Subscripts

e = exterior value
h = hexagon
i = interior value
p = pentagon
$\bar{z}$ = complex conjugate of z

Appendix A: FEM Convergence

A.1 Rectangles. For a rectangle with isothermal sides of width a and adiabatic sides of height b, the interior shape factor is exactly $S_i = a/b$. The exterior shape factor was computed using MATLAB's FEM tools. Mesh convergence was evaluated by reducing the maximum mesh size, $H_{\max}$, until machine memory limits were exceeded (Table 5). Localized mesh refinement was applied at each outside vertex and edge, limiting the maximum mesh to $H_{\max}/40$. The computation is sensitive to the outer boundary condition of the domain, which was set to a circle of radius 20. The far-field temperature was shown to limit to a dipole distribution in Ref. [4], and that boundary condition was used on the outside edge.

The heat flow was determined by integrating the computed heat flux along the bottom edge. The heat flux has an integrable singularity at each vertex ($x = \pm 1$), so corner corrections were applied as described in Ref. [4]. Specifically, the computed heat flux normal to the bottom boundary was fit the first and third terms of the expansion for corner singularities (Eq. (68) in Ref. [4])

$$\left|\frac{\partial T}{\partial n}\right| = A\eta_1(1+x)^{\eta_1-1} + B\eta_1(1-x)^{\eta_1-1} + C(5\eta_1)(1+x)^{5\eta_1-1} + D(5\eta_1)(1-x)^{5\eta_1-1} \tag{A1}$$

where x is the coordinate along the bottom wall, $\eta_1 = K/[2(K+2)]$ for a regular K-gon or a rectangle ($K = 4$), and A, B, C, D are fitting coefficients. When curve fitting the flux and when integrating for the shape factor S, both ends of the bottom edge are omitted over a distance $\delta x = H_{\max}/2$, based on the observed break-down of the flux calculation near the endpoints. Integrating the fitted flux distribution, a distance δx from each corner gives

$$\Delta S \Delta T \cong (A+B)(\delta x)^{\eta_1} + (C+D)(\delta x)^{5\eta_1} \tag{A2}$$

for $k = 1$. We then add ΔS to S.

The horizontal dimension of the rectangle was held fixed at $a = 2$ and b was varied. Table 5 shows the results. The computed value for $a/b = 1$ is within 0.5% of the exact value, 1, when $H_{\max} = 0.02$. Obviously, $S_e(a/b) = 1/S_e(b/a)$. This relationship is satisfied to about 1% over the range considered. For the two largest a/b, the convergence is less, but likely better than 2%. The values for $H_{\max} = 0.02$ are plotted in Fig. 1. In these calculations, the far-field dipole temperature distribution was based on a strength $2S_e$ at a separation b.

A.2 Regular *K*-Gons. The exterior shape factors were computed using the same procedure as for the rectangles (with accommodations for the S_h^{2-2} hexagon, Fig. 4, in which an isothermal edge adjoins the bottom edge). The exterior results are within 1.4% of the interior FEM results. The specific choice of outer boundary condition (isothermal, adiabatic, or dipole) affects the results. For the maximum radii and minimum mesh sizes achievable, isothermal outer boundaries run a fraction of a percent higher than dipole boundaries, and adiabatic boundaries run lower by 1–1.5%.

Table 5 Exterior shape factor S_e for a rectangle of width a and height b, by FEM. For the interior, $S_i = a/b$.

		a/b $(= S_i)$						
	$H_{\max}$	0.25	0.5	1	2	4	8	16
S_e	0.05	0.7496	0.8584	0.9885	1.138	1.301	1.471	1.637
	0.02	0.7535	0.8637	0.9948	1.146	1.314	1.491	1.670

Far field has a dipole temperature distribution at radius 20.

The interior FEM calculations were straightforward, and comparison to known exact values and reciprocal relationships, together with grid convergence studies, places their accuracy at about 0.05%. The reciprocal relationship [6] states that, when isothermal and adiabatic boundaries are interchanged, the resulting shape factor is the reciprocal of the original shape factor. Thus, in Fig. 4, the following relationships are met, as is evident upon comparison of the respective flux plots: $S_p^{1-1} = 1/S_p^{2-1}$, $S_h^{1-1} = 1/S_h^{2-2}$, and$S_h^{1-1R} = 1/S_h^{3-1}$. The reciprocal values agree to 0.05–0.1%.

For $K > 4$, the interior flux has a weak singularity at corners that join isothermal and adiabatic segments, but grid refinement was sufficient to account for these. For the hexagon with half of a side isothermal (Table 1, last item), a stronger interior singularity is present at the transition point from isothermal to adiabatic (see Ref. [4], Sec. 6.2), and a numerical correction was applied using methods similar to Appendix A.1.

Appendix B: Schwarz–Christoffel Mappings for Regular *K*-Gons

The interior Schwarz–Christoffel mapping, in general, is

$$f(z) = c_1 \int_0^z \frac{dz}{(b_1 - z)^{\mu_1} \cdots (b_K - z)^{\mu_K}} + c_2 \tag{B1}$$

where c_1 and c_2 are constants [11]. The mapping of the interior of the unit disk to either the interior or the exterior of a regular K-gon uses as prevertices the K roots of unity, $b_k = \exp(2\pi i k/K)$. The exterior angles of the K-gon are $\pi\mu_i = 2\pi/K$. With

$$\prod_{k=1}^{K}(b_k - z) = \prod_{k=1}^{K}(e^{2\pi i k/K} - z) = (1 - z^K) \tag{B2}$$

the mapping of the unit disk to the interior of a regular K-gon reduces to

$$f(z) = \int_0^z \frac{dz}{(1 - z^K)^{2/K}} \tag{B3}$$

where we take $c_1 = 1$ and $c_2 = 0$.

The mapping of the disk interior to the exterior of a polygon is

$$f(z) = c_3 \int_{z_0}^{z} \frac{(b_1 - z)^{\mu_1} \cdots (b_K - z)^{\mu_K}\, dz}{z^2}, \quad z_0 \neq 0 \tag{B4}$$

with c_3 a constant [11]. We have the same prevertices and exterior angles as for the interior case. With $c_3 = 1$, the mapping of the disk to the exterior of the K-gon is

$$f(z) = \int_{z_0}^{z} \frac{(1 - z^K)^{2/K}\, dz}{z^2}, \quad z_0 \neq 0 \tag{B5}$$

Since the same points, the prevertices, are conformally mapped to the vertices of either the interior or exterior K-gon, and since isotherms map to isotherms and adiabats to adiabats, the boundary conditions are identical for the interior and exterior problems. It follows immediately see that the shape factor, a conformal invariant, is the same for the interior and the exterior problems on the K-gon. (Note that we have not shown that the interior and exterior K-gons have the same dimensions or the same vertices—neither question is relevant to our result.)

Appendix C: Proof of Eq. (3)

We first note that the shape factor for the disk problem in Fig. 8 was given by Hersch [6] as

$$S(\alpha) = \frac{K(s)}{K\left(\sqrt{1-s^2}\right)} \tag{C1}$$

where

$$s = \sin\left(\frac{\alpha}{2}\right) \tag{C2}$$

(The shape factor is the inverse of Hersch's conformal modulus.) Equation (C1) is readily evaluated to find the shape factor for any angle α.

Now consider a quadrilateral with N-fold symmetry, where boundary conditions do not change along each primitive edge. Four points demarcate the junctions of isothermal and adiabatic sections on the quadrilateral. By the construction of Sec. 3, each primitive edge of the shape under consideration will be mapped onto a segment on the unit disk spanning $2\pi/N$ rad. This mapping takes four boundary points on the quadrilateral onto four distinct points of the form $\exp(\mathrm{i}2\pi m/N)$. The four values of m are determined as follows. Suppose that, in clockwise order, the boundary conditions are N_H primitive sides isothermal at T_1, followed by N_A adiabatic primitive sides, followed by N_C primitive sides isothermal at T_2, followed by $N-(N_H+N_A+N_C)$ adiabatic sides. Then, the four boundary points are located at $z_1 = 1$, $z_2 = \exp(-\mathrm{i}2\pi N_H/N)$, $z_3 = \exp\left[-\mathrm{i}2\pi(N_H+N_A)/N\right]$, and $z_4 = \exp\left[-\mathrm{i}2\pi(N_H+N_A+N_C)/N\right]$.

For some value of α, the unit disk can be mapped onto itself while taking each boundary point of the quadrilateral to the four boundary points in Fig. 8. Since the Riemann mapping theorem only allows one to set the image of three points, the mapping is only possible for a specific value of α that is determined as follows.

We first note that the cross-ratio of four points on the boundary, defined as

$$\mathrm{CR}(z_1,z_2,z_3,z_4) = \frac{(z_1-z_3)(z_2-z_4)}{(z_1-z_4)(z_2-z_3)} \tag{C3}$$

is invariant under linear fractional transformations [14]; a subclass of such transformations map the unit circle to itself. One such transformation takes our quadrilateral domain onto the domain depicted in Fig. 8 for a particular value of α that we shall now deduce. Proceeding clockwise on the geometry of Fig. 8, the cross-ratio is calculated using $z_1 = \exp(\mathrm{i}\alpha)$, $z_2 = 1$, $z_3 = -\exp(\mathrm{i}\alpha)$, and $z_4 = -1$. We find $\mathrm{CR} = \sec^2(\alpha/2)$. Meanwhile, the cross-ratio for a body with N-fold symmetry is

$$\mathrm{CR} = \frac{\sin\left(\frac{(N_A+N_C)\pi}{N}\right)\sin\left(\frac{(N_A+N_H)\pi}{N}\right)}{\sin\left(\frac{N_A\pi}{N}\right)\sin\left(\frac{(N_A+N_C+N_H)\pi}{N}\right)} \tag{C4}$$

For the appropriate value of α, these cross-ratios must be equal, revealing the identity

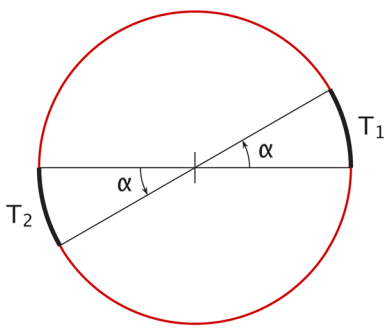

Fig. 8 Disk with isothermal sectors of angle α

$$C^2 = \cos^2\left(\frac{\alpha}{2}\right) = \frac{\sin\left(\frac{N_A\pi}{N}\right)\sin\left(\frac{(N_A+N_C+N_H)\pi}{N}\right)}{\sin\left(\frac{(N_A+N_C)\pi}{N}\right)\sin\left(\frac{(N_A+N_H)\pi}{N}\right)} \tag{C5}$$

where we define C^2 as shown. With $\cos^2(x) = 1-\sin^2(x)$, we obtain

$$S(N_H,N_A,N_C,N) = \frac{K\left(\sqrt{1-C^2}\right)}{K(C)} \tag{C6}$$

where

$$C = \sqrt{\frac{\sin\left(\frac{N_A\pi}{N}\right)\sin\left(\frac{(N_A+N_C+N_H)\pi}{N}\right)}{\sin\left(\frac{(N_A+N_C)\pi}{N}\right)\sin\left(\frac{(N_A+N_H)\pi}{N}\right)}} \tag{C7}$$

Appendix D: A Short Catalog of Results

In this appendix, we provide a brief tabulation of shape factors for a few additional objects for which interior and exterior shape factors are equal. This catalog is by no means exhaustive.

Yin–Yang bodies. A Yin–Yang body has an axis of symmetry about which isothermal and adiabatic boundaries are interchanged (Sec. 4.6). Every Yin–Yang body is conformally equivalent to a square and has $S_i = S_e = 1$.

Disks. A disk with symmetric isothermal angular sectors is shown in Fig. 8. Equation (C1) provides the shape factor as a function of the angle α. Shape factors for several angles are given in Table 6; and the angles that yield several shape factors are given in Table 7. For all disks, $S_i \equiv S_e$.

The case $\alpha = 30$ deg has the analytical solution $S = 1/\sqrt{3}$ [6]; and, because the case $\alpha = 150$ deg simply interchanges the boundary conditions, reciprocity [6] shows it to have the analytical solution $S = \sqrt{3}$. Similarly, the shape factor for α is the reciprocal of the shape factor for 180 deg $-\alpha$. The case $\alpha = 90$ deg is a Yin–Yang body with $S = 1$. The results are accurate to the number of digits shown in the tables.

Regular K-gons. Interior flux plots for all unique regular pentagon and regular hexagon problems are shown in Table 3. The isothermal sides are indicated with heavy lines, and the other sides are adiabatic. In all cases, the bottom side has a different temperature than the top sides. The specific boundary conditions are apparent from the flux plots. The exact shape factors from Eq. (3) are shown alongside the numerical results obtained through FEM analysis.

Table 6 Shape factor for various angles on a symmetric sector disk (numerical details in Appendix A)

α (deg)	90.00	75.00	60.00	45.00	30.00	15.00
S	1.0000	0.8865	0.7817	0.6806	$1/\sqrt{3}$	0.4595
α (deg)	90.00	105.00	120.00	135.00	150.00	165.00
S	1.0000	1.1280	1.2793	1.4692	$\sqrt{3}$	2.1761

Table 7 Angle producing various shape factors on a symmetric sector disk

S	1.0000	1.5000	2.0000	3.0000	5.0000
α (deg)	90.00	137.07	160.24	175.88	179.82
S	1.0000	0.7500	0.5000	0.3000	0.2000
α (deg)	90.00	55.32	19.76	2.439	0.01779

The FEM results are accurate to 0.03% or better. The exact value for S_h^{2-1} stems from the Yin–Yang symmetry, while the exact result for S_h^{2n-1} is due to Hersch [6].

The exterior shape factors were computed numerically and, in each case, we found an agreement of 1.4% or better with the interior FEM value; the difference is within the accuracy of the exterior computation. (FEM convergence was discussed in Appendix A.) These results support the equality of interior and exterior shape factors for regular K-gons, and they serve to further confirm Eq. (3).

Shape factors on half-squares. If each side of a square is divided into two equal parts, we have eightfold symmetry. Consider the shape factor when two half-sides are at different temperatures and are separated by one or more adiabatic sides. Four unique arrangements exist, with other arrangements being simple rotations of the others.

To construct the four unique cases, we hold the bottom-left half-side at T_1 and vary the side at T_2. Table 4 shows the possible combinations with the interior shape factors calculated by FEM as before.

Cases TL and UR both have $S_i = 1/\sqrt{2}$ because these two shapes are conformally equivalent. By mapping the square problems onto the unit circle, using the method laid out in Sec. 3, it is readily seen that both TL and UR correspond to the same problem on the unit circle and are thus conformally equivalent. Conformally equivalent problems have the same shape factor.

The half-square geometry is also conformally equivalent to an octagon. Therefore, these shape factors also apply to octagons with two isothermal faces separated by the appropriate number of adiabatic faces.

References

[1] Yovanovich, M. M., 1998, "Conduction and Thermal Contact Resistances (Conductances)," *Handbook of Heat Transfer*, 3rd ed., W. M. Rohsenow, J. P. Hartnett, and Y. I. Cho, eds., McGraw-Hill, New York, Chap. 3.

[2] Lienhard, J. H., IV, and Lienhard, and J. H., V, 2019, *A Heat Transfer Textbook*, 5th ed., Dover Publications, Mineola, NY.

[3] Hahne, E., and Grigull, U., 1975, "Formfaktor und Formwiderstand der stationären mehrdimensionalen Wärmeleitung," Int. J. Heat Mass Transfer, **18**(6), pp. 751–767.

[4] Lienhard, J. H., 2023, "Steady Two-Dimensional Conduction: Simple and Double Layer Potentials, Corner Singularities, and Induced Heat Flux," ASME J. Heat Mass Transfer-Trans. ASME, **145**(3), p. 031401.

[5] Ahlfors, L. V., 2010, *Conformal Invariants: Topics in Geometric Function Theory*, Vol. 371, AMS Chelsea Publishing, American Mathematical Soc., Providence, RI, pp. 48 and 65.

[6] Hersch, J., 1982, "On Harmonic Measures, Conformal Moduli and Some Elementary Symmetry Methods," J. Anal. Math., **42**(1), pp. 211–228.

[7] Hersch, J., 1987, "On the Mapping Functions of Domains Extended by Sector Reflections," Complex Var. Elliptic Equations, **9**(2–3), pp. 199–209.

[8] Lienhard, J. H., 2019, "Exterior Shape Factors From Interior Shape Factors," ASME J. Heat Mass Transfer-Trans. ASME, **141**(6), p. 061301.

[9] Gamelin, T. W., 2003, *Complex Analysis*, Springer Science & Business Media, New York, pp. 283 and 290.

[10] Lienhard, J. H., 1981, "Heat Conduction Through "Yin-Yang" Bodies," ASME J. Heat Mass Transfer-Trans. ASME, **103**(3), pp. 600–601.

[11] Nehari, Z., 1952, *Conformal Mapping*, McGraw-Hill Book Company, New York.

[12] Borwein, J. M., and Borwein, P. B., 1987, *Pi and the AGM: A Study in the Analytic Number Theory and Computational Complexity*, Wiley-Interscience.

[13] Gopal, A., and Trefethen, L. N., 2019, "Solving Laplace Problems With Corner Singularities Via Rational Functions," SIAM J. Numer. Anal., **57**(5), pp. 2074–2094.

[14] Ahlfors, L. V., 1979, *Complex Analysis: An Introduction to the Theory of Analytic Functions of One Complex Variable*, 3rd ed., McGraw-Hill, New York, p. 78.